Cell Reports
Physical Science

Article

4D multimodal neutron and X-ray tomography of lithium transport in all-solid-state batteries using Li-7 contrast enhancement

Graphical abstract

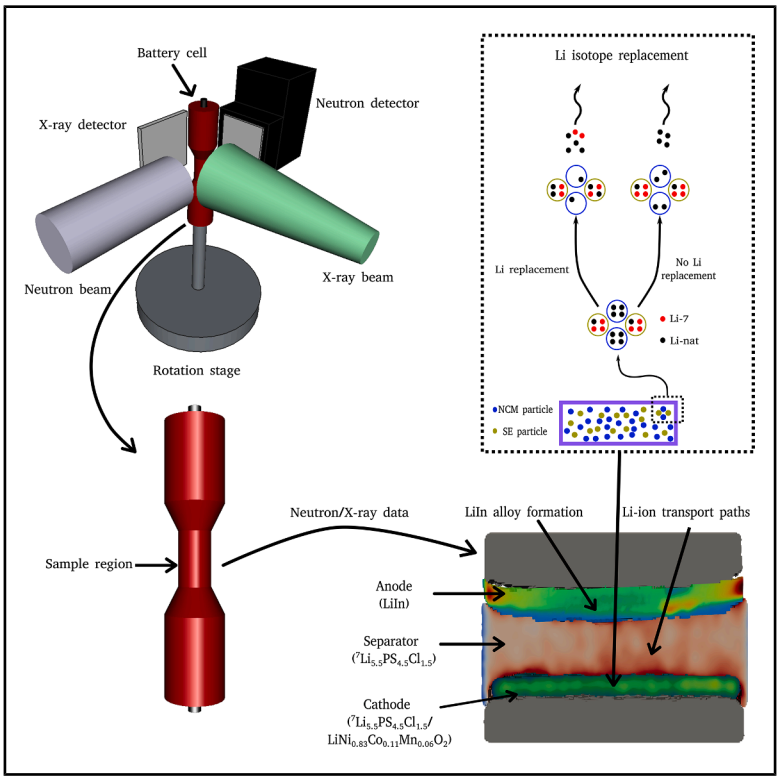

Highlights

- Neutron tomography reveals localised lithium-ion diffusion in the separator
- Combined neutron and X-ray tomography reveal inhomogeneous LiIn alloy formation
- Lithium concentration gradients in the cathode are observed during delithiation
- The lithium isotope distribution in the separator is quantified using isotope mapping

Authors

Philip Vestin, Eva Schlautmann, Oriol Sans-Planell, ..., Alessandro Tengattini, Wolfgang G. Zeier, Stephen Hall

Correspondence

philip.vestin@solid.lth.se

In brief

Vestin et al. employ neutron and X-ray tomography in combination with lithium isotope mapping to study the lithium-ion diffusion in all-solid-state lithium-ion batteries. The results reveal localized lithium diffusion through the separator, as well as lithium concentration gradients in the cathode developing during charging.

Vestin et al., 2026, Cell Reports Physical Science 7, 103136
February 18, 2026
https://doi.org/10.1016/j.xcrp.2026.103136

CellPress

Cell Reports
Physical Science

CellPress
OPEN ACCESS

Article

4D multimodal neutron and X-ray tomography of lithium transport in all-solid-state batteries using Li-7 contrast enhancement

Philip Vestin,[1,9,*] Eva Schlautmann,[2] Oriol Sans-Planell,[3] Nikolay Kardjilov,[3] Robin Woracek,[4] Alessandro Tengattini,[5,6,7] Wolfgang G. Zeier,[2,8] and Stephen Hall[1]

[1]Lund University, Division of Solid Mechanics, Lund, Sweden
[2]Institute of Inorganic and Analytical Chemistry, University of Münster, Münster, Germany
[3]Helmholtz-Zentrum Berlin für Materialien und Energie, Berlin, Germany
[4]European Spallation Source ERIC, Lund, Sweden
[5]Institut Laue-Langevin, 71 Avenue des Martyrs, Rhône-Alpes, 38042 Grenoble, France
[6]University Grenoble Alpes, Grenoble INP, CNRS, 3SR, 1270 Rue de la Piscine, 38400 Grenoble, France
[7]Institut Universitaire de France (IUF), Paris, France
[8]Forschungszentrum Jülich GmbH, Institute of Energy Materials and Devices Helmholtz-Institute Münster (IMD-4), 52425 Jülich, Germany
[9]Lead contact
*Correspondence: philip.vestin@solid.lth.se
https://doi.org/10.1016/j.xcrp.2026.103136

SUMMARY

This paper explores the use of multimodal X-ray and neutron operando tomography to study all-solid-state lithium-ion batteries (ASSBs). The use of operando neutron tomography as a method for quantifying the local lithium distribution in battery cells under charging is explored in conjunction with the use of simultaneous operando X-ray tomography to obtain complementary information about the internal battery structure. It is demonstrated how the components of an ASSB can be segmented in the dual modality images to reveal the topology of the electrodes. Next, 4D mapping of the lithium isotope content in the separator revealed spatial inhomogeneities in the distribution of Li-6 and Li-7. Furthermore, the delithiation process in the cathode of an ASSB has been followed in 4D, revealing lithium concentration gradients in the cathode, even with the slow delithiation rate used in the experiment.

INTRODUCTION

All-solid-state batteries (ASSBs) are promising candidates for future energy storage systems. There have been an increasing number of studies to ensure the performance and safety of these batteries. Such studies are often based on electrochemical bulk measurements. With this comes an inherent assumption of a one-dimensional (1D) battery structure and 1D diffusion processes, i.e., that the electrode and separator layers are homogeneous and that the processes occurring within the cell develop homogeneously within these layers. This inherent assumption stems from the lack of measurements of the internal battery structures and their evolution. Heterogeneity is often pronounced in ASSBs due to the mechanical loading necessary for the battery material consolidation and the requirement to operate under pressure to facilitate the diffusion processes. In recent years, tomographic X-ray imaging studies have revealed the heterogeneous nature of the structures and processes of lithium-ion batteries (e.g., Kodama et al.,[1] Lübke et al.,[2] and Ziesche et al.[3]). While X-ray tomography has been shown to be a powerful tool in the study of internal battery processes, including for lithium-based batteries and ASSBs, the tracking of lithium ion diffusion is challenging due to the low interaction of X-rays with lithium, especially in the presence of more highly interacting materials. Neutron imaging provides a strong sensitivity to lithium and has, thus, been cited as an ideal tool in lithium-ion battery studies.[4] It is also possible, with neutron imaging, to differentiate different isotopes of lithium, since Li-6 strongly absorbs neutrons, whereas Li-7 has a significantly lower neutron absorption cross-section, enabling isotope-specific tracking of lithium ion diffusion through battery cells (see Bradbury et al.[5,6] and Magnier et al.[7]). However, the limited neutron flux at most neutron facilities has restricted the possibility for operando 4D studies (i.e., 3D imaging during charge/discharge) such that studies have involved just 2D operando neutron radiography or limited 3D imaging either before or after charging.[2,5,6] Furthermore, in some cases, the neutron attenuation coefficients of materials in the battery are similar, such that they cannot be easily identified and separated from neutron tomography images alone. In this case, dual-modality X-ray and neutron tomography can provide complementary images of the same cell and enable segmentation of the battery components based on both images, profiting from the different material interactions of the two modalities.

This paper showcases the potential of using neutron tomography, coupled with X-ray tomography and lithium isotope mapping, to assess the operational performance of ASSBs and to

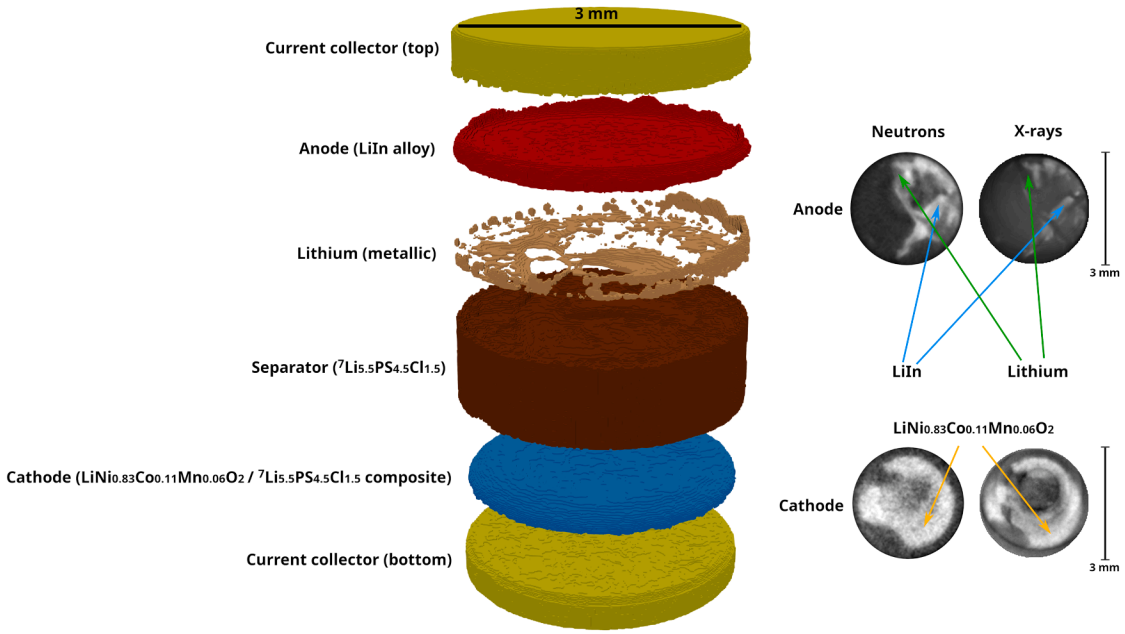

Figure 1. Rendering of the segmented image volume from the registered neutron and X-ray tomography data of cell A

The segmented regions are expanded vertically for clarity. The horizontal slices on the right show how the anode and cathode (all slices shown at the interface with the separator) appear in the different modalities.

understand the heterogeneity of the processes involved in charge and discharge. Here, we exploit the high neutron flux and dual-modality imaging available at the NeXT beamline[8] of the Institut Laue-Langevin to reveal the details of the ASSB battery evolution in 3D, avoiding uncertainties in the interpretation present in 2D radiographic measurements. The studied ASSB cells had lithium-indium (LiIn) anodes, separators consisting of a lithium argyrodite ($^7Li_{5.5}PS_{4.5}Cl_{1.5}$) solid electrolyte (SE), and cathodes consisting of a composite of NCM ($LiNi_{0.83}Co_{0.11}Mn_{0.06}O_2$) and SE. The lithium in the SE was enriched with the Li-7 isotope, which provided contrast in the neutron tomography images compared to regions with natural lithium (due to the different Li-6 and Li-7 concentrations and their different neutron absorption properties). This contrast enabled us to track the diffusion path of natural lithium ions from the cathode into the separator using neutron tomography data. Thus, using the operando spatiotemporal (4D) neutron imaging and isotope mapping, three key processes have been studied in the ASSB cells: (1) lithium ion diffusion through the separator; (2) lithium ion intercalation and deintercalation in the NCM/SE composite cathode; and (3) electrochemically driven alloy formation in the LiIn anode where indium has been used to stabilize the lithium metal in the presence of the SE separator. Understanding these processes is key to mitigating ASSB capacity loss. In particular, data on the battery structure and heterogeneity and on how these two influence lithium ion migration are necessary for developing effective strategies and accurate models for battery design and optimization. Additionally, it is shown how multimodal neutron and X-ray imaging can be used to obtain a segmented volume from one of the studied battery cells, revealing an inhomogeneous distribution of lithium and indium in the anode, something that would have been difficult to identify using neutron tomography only. Crucially, little is known about the evolution of the microstructure of LiIn alloy anodes during charge/discharge, and the effects of heterogeneity in the distribution of lithium and indium.

The results are presented for two cells: cell A where the internal battery evolution has been followed during 3.5 charge-discharge cycles and cell B where the data focuses on the initial charge cycle only. Consequently, it is possible to assess the application of neutron imaging to follow charge cycling with cell A and details on initial charging and quantification of the state of lithiation are possible for cell B. The presentation of the results for the two cells is followed by a discussion on the use of *in situ*, operando studies of lithium battery processes with neutron tomography and isotope mapping. The experimental method is presented in detail in the methods section at the end of the paper.

RESULTS

In the first part of this study, multimodal neutron and X-ray tomography is used to segment the different components of cell A, revealing an inhomogeneous distribution of lithium and indium in the anode. The evolution of the LiIn alloy has then been followed using the neutron tomography data. Additionally, the lithium isotope distribution in the separator of cell A has been characterized using operando neutron tomography and lithium isotope contrast enhancement. We present the results from this study and highlight what can (and what cannot) be determined from the approach.

The second part of the paper is focused on lithium-ion diffusion in the cathode of an ASSB (cell B) throughout the initial

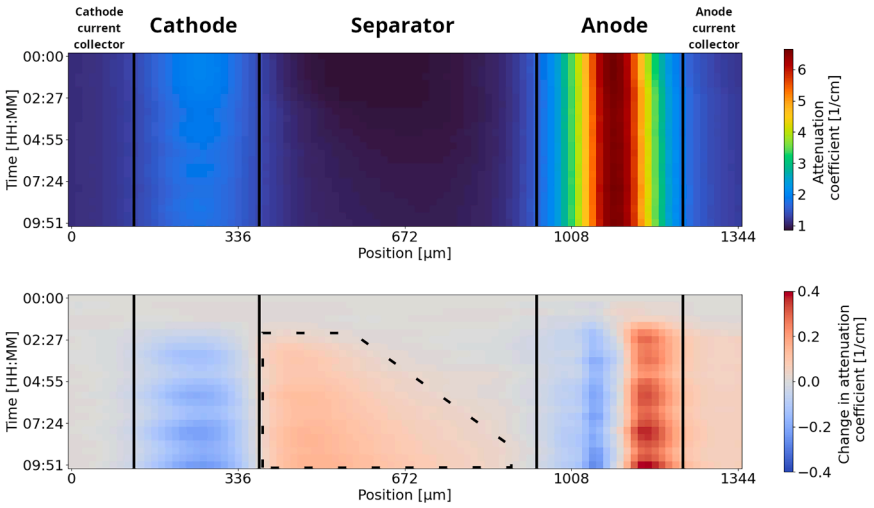

Figure 2. Cell A: Intensity plots of the neutron attenuation coefficient and the change in neutron attenuation coefficient

The top panel shows the neutron attenuation coefficient, and the bottom panel shows the change in neutron attenuation coefficient, which is measured relative to the initial state. The data are given as functions of the position along the cell symmetry axis from the cathode current collector, and of time from the start of the tomographic scans. The area marked with dashed lines shows the evolution over time of the Li-6 concentration in the separator.

delithiation. By using a low current, the delithiation process could be studied using neutron tomography while maintaining a high relative temporal resolution.

Cell A: Multimodal imaging and lithium isotope distribution

By combining the 3D neutron and X-ray tomography data, it is possible to exploit the different material sensitivities of the two techniques and segment the dual-modality image into the sample materials to identify the different volumes of each constituent. This procedure involves aligning (registering) the X-ray and neutron tomographies and defining regions in the "dual-histogram" of the intensities in the two images that correspond to the different components (segmentation); see for example Roubin et al.[9] Figure 1 shows an example of the result of the registration and segmentation of the multimodal tomography data for cell A with the different material volumes highlighted. The different components of the cell, such as the separator, the anode, and the cathode, can be distinguished clearly from each other, thanks to their difference in neutron and X-ray attenuations. By using multimodal segmentation, it is possible to distinguish regions in the anode consisting primarily of lithium from regions consisting of indium or LiIn. If only X-ray tomography is used, low-attenuation regions cannot be reliably identified as either lithium or voids. Such voids may form when the lithium and indium foils fold or wrinkle during assembly. Although a difference in neutron attenuation between the lithium regions and the indium/LiIn regions is possible to observe, it is not obvious to realize that it is caused by phase segregation using only the neutron tomography data. Thus, the combined dataset is needed to understand the observations.

The quantification of the lithium isotope distribution in the separator has been achieved by analysis of the image intensities in the neutron tomography data. As the separator was synthesized with Li-7 (an isotope with low neutron attenuation), the natural lithium ions that diffused between the electrodes could be identified in the separator due to the greater neutron attenuation of natural lithium relative to the Li-7 initially present in the separator. This contrast enhancement allowed the creation of a spatiotemporal map of the lithium isotope distribution by correlating the measured neutron attenuation to the lithium content using the theoretical neutron attenuation coefficients of the elements in the separator, as described in the methods section.

Lithium intercalation in the cathode and LiIn alloy formation in the anode

Figure 2 shows the neutron attenuation profiles, as a function of position along the cell axis, of cell A for each tomography through the charge cycling. These profiles are based on the integration of the neutron attenuation perpendicular to the axis of symmetry of the cell. The profiles reveal that the neutron attenuation in the cathode changed in a cyclic manner over time, indicating changes between a state of lithiation (higher relative attenuation) and a state of delithiation (lower relative attenuation). In the separator, the neutron attenuation increased over time, which is a result of the more attenuating natural lithium ions from the cathode being transported through the Li-7-enriched separator.

The evolving gradient in neutron attenuation away from the cathode through the separator indicates a diminishing Li-6 concentration in the separator toward the anode over a region that expands with the cycling (marked with dashed lines in Figure 2), as the Li-6 replaces the Li-7 (which exists initially in excess in the separator). Conversely, the neutron attenuation can be seen to have decreased in the cathode, which is interpreted as being due to the amount of Li-6 in the cathode decreasing (non-monotonously) over time.

At the anode current collector, an increase in the neutron attenuation coefficient can be observed approximately 2.5 h into the measurement. The reconstructed X-ray tomography images also indicate an increase in attenuation in this region, suggesting that indium-rich material is either creeping between the current collector and the inner walls of the battery cell or is electrochemically deposited onto the side of the current collector. It is not possible to determine the exact composition of the material from the available data, but, as it is possible to observe in the reconstructed X-ray tomographies, it must contain indium rather than only lithium.

As the lithium ions from the cathode passed through the separator, they are expected to have plated onto or alloyed with the LiIn anode. The increase in neutron attenuation at the interface between the anode and the anode current collector in Figure 2

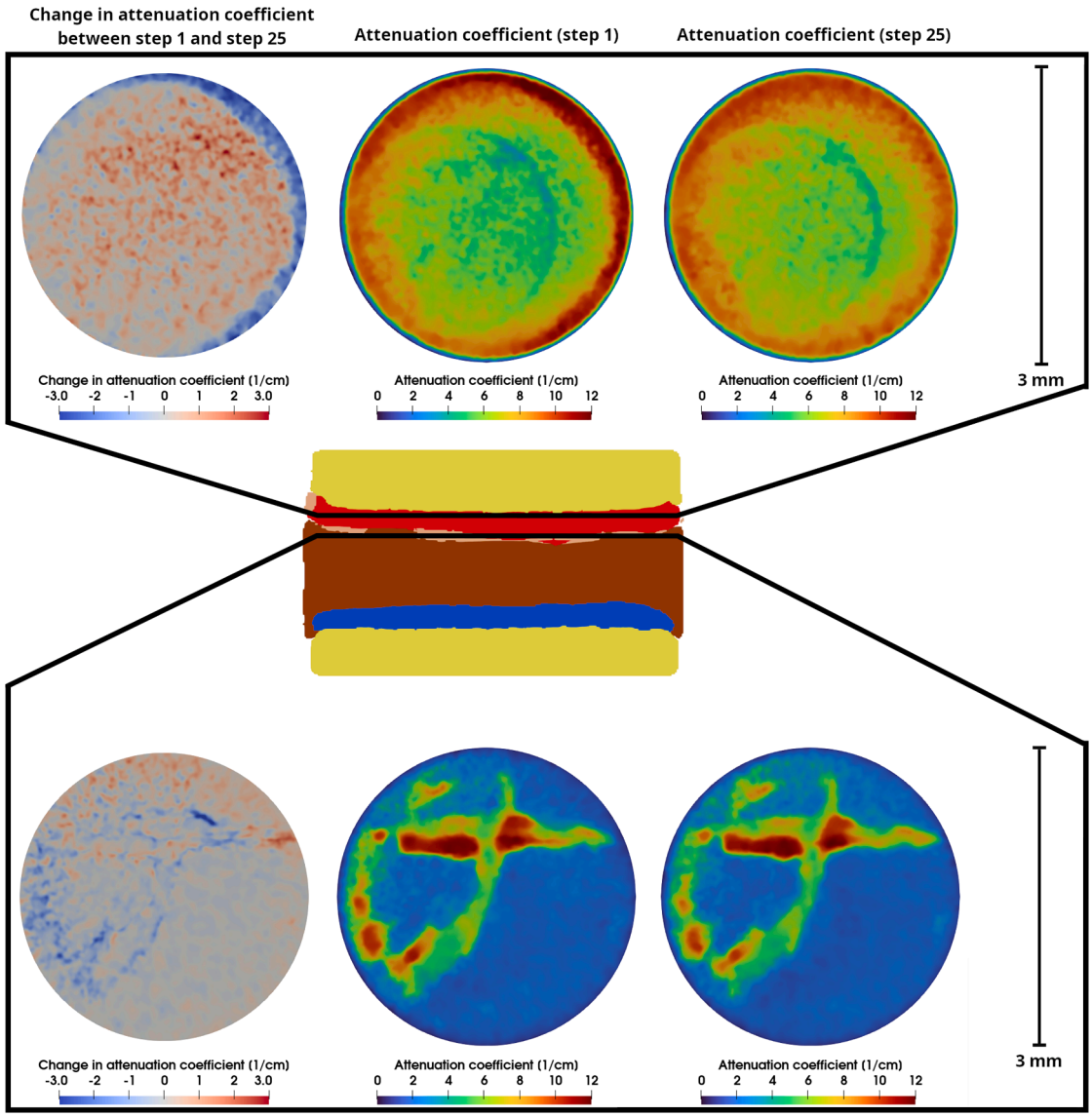

Figure 3. Cell A: Neutron attenuation coefficient at the first time step (step 1), the last time step (step 25), and the change in neutron attenuation coefficient between step 1 and step 25

The data are shown for slices at the center of the anode (top) and at the interface between the anode and the separator (bottom). The left column shows the change in attenuation coefficient between step 1 and step 25, the center column shows the attenuation coefficient at step 1, and the right column shows the attenuation coefficient at step 25.

suggests that the anode either expanded toward the current collector by filling any space between the anode foil and the steel current collector pin or became more attenuating as a result of electrochemically driven structural changes in the LiIn alloy itself. By comparing the change in the neutron attenuation coefficient relative to the position of the LiIn foil in Figure 2, it is revealed that changes in the neutron attenuation occurred both on the side of the anode adjacent to the separator and on the side adjacent to the current collector. The increase in neutron attenuation on the side of the anode adjacent to the current collector appears to oscillate at the same rate as the lithiation-induced attenuation variations in the cathode, suggesting that the increase in attenuation at the anode is related to the formation of LiIn alloy in the anode on lithiation and the subsequent decomposition of the alloy on delithiation.[10,11] Examining the neutron attenuation in horizontal slices of the anode, shown in Figure 3, it is seen that regions of high neutron attenuation, indicative of a high indium content, become less attenuating during the cycling. The opposite happens for regions in the anode with a lower neutron attenuation, indicating a high lithium content. Since this evolution is observed in the bulk of the anode and not only on the surface of the anode, these observations support the hypothesis of a

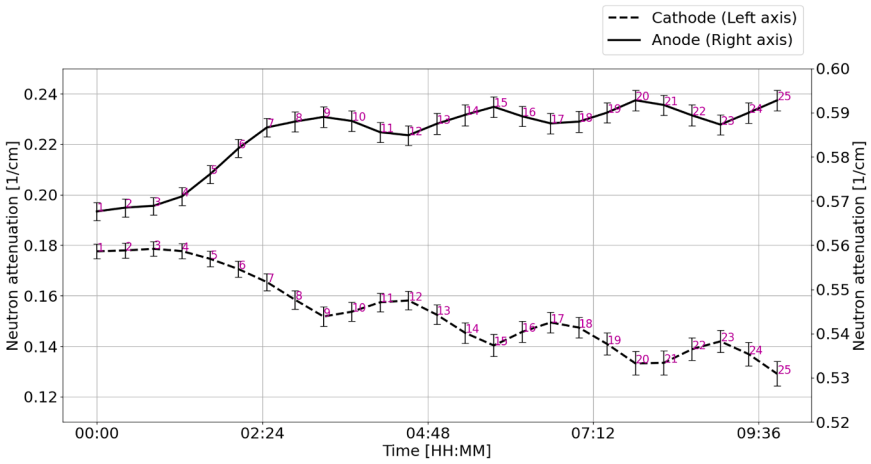

Figure 4. Cell A: Average attenuation coefficient of the cathode and anode

The attenuation coefficient is averaged over the volume of the entire battery. The numbers denote the points at which tomographies were performed and correspond to the numbering used in Figures 5 and 6. Note how the attenuation of the cathode and the anode are anti-correlated due to the cyclic lithium ion transfer between the electrodes. The error bars show the change from a ±1% change in the segmentation threshold.

continued LiIn alloy formation and phase equilibration during cycling.

The non-monotonous decrease in neutron attenuation in the cathode, shown in Figure 2, and its correlation with the changes in neutron attenuation on the anode side have been further studied by segmenting the anode and cathode from the reconstructed neutron tomographies. Since the anode expands and contracts with the charge cycles, the average neutron attenuation is measured relative to the entire cell volume, to avoid changes in neutron attenuation being canceled by the corresponding changes in volume. The average neutron attenuation over time for the anode and the cathode, shown in Figure 4, shows how the changes in neutron attenuation of the two electrodes are anti-correlated in time, which reflects the expected correlation between the delithiation of the cathode and the lithium increase in the anode implied in Figure 2.

While the initial delithiation of the cathode appears to be significantly slower than the subsequent cycles, there is no noticeable phase shift between changes in the cathode and changes in the anode. Nevertheless, Figure 4 reveals a noticeable net increase in the average neutron attenuation of the anode, especially after the first initial charge. This indicates that as the cell was cycled, the amount of lithium in the anode increased with every cycle, suggesting that there is capacity loss in the cell, since not all the lithium that was removed from the cathode when charging is retrieved from the anode upon discharge.

Quantification of Li-6 concentration

In the above, we maintain the commonly held assumption that lithium ion diffusion is essentially a 1D process. Nevertheless, this 4D dataset allows the validation of this assumption by studying the reconstructed spatiotemporal Li-6 distribution as a series of 3D volumes, as shown in Figure 5. This reveals that there is a region of higher Li-6 content already in the separator in the first tomography, i.e., before the start of the cycling. This region must have formed before the first charge, i.e., between the assembly of the cell and the start of the experiment. By examining the temporal variation of the Li-6 distribution, it is evident that there is a net increase in Li-6 content across the entire separator, over all the cycles. This suggests that this preferential diffusion path for the lithium ions that caused the Li-6 distribution to localize does not prevent the entire electrolyte from being utilized to some degree during cycling of the battery.

As the battery is cycled, the neutron attenuation of the separator increases over time, due to the diffusion of natural lithium ions into the separator. This causes a net increase in the Li-6 content by replacing the excess Li-7 in the separator with Li-6 from the natural lithium present in the NCM and in the anode. This process is not reversible, as seen in Figure 5 and the attenuation profiles shown in Figure 2, where it can be noted that the neutron attenuation of the separator does not return to its original value between cycles. Therefore, the isotope contrast enhancement does not reveal how the lithium ions may have diffused during any particular cycle, beyond the first delithiation of the cathode. It also implies that over time, the lithium isotope distribution of the separator would reach some steady-state value, once the lithium isotope distribution has become homogenized.

Since the region of high Li-6 concentration on the right side of the separator, highlighted in Figure 5, already had a Li-6 content at the start of the experiment that was close to the Li-6 content of natural lithium, any changes in that region are less evident. To identify the areas with the maximum variation of Li-6, the spatiotemporal Li-6 distribution can be measured relative to the initial state, as shown in Figure 6. This reveals that the greatest change in Li-6 content is not located in the same region where the initially largest amount of Li-6 was observed. These data show that regardless of which measure is considered, the absolute lithium concentration or the change relative to the initial state, the lithium ion diffusion followed preferential pathways through the separator, rather than diffusing as a homogeneous front. The localized diffusion front may have a number of different causes, including inhomogeneous mixing of the separator material during production, an inhomogeneous pressure distribution in the cell leading to spatial differences in the ionic conductivity of the separator, or an inhomogeneous electric field in the cell, caused by the uneven morphology of the electrodes.

State-of-charge quantification: Cell B

For cell B, to focus on the 3D lithium-ion transport in the cathode using lithium isotope mapping, only the change from the pristine discharged state to the charged state was investigated. A lower current density was applied compared to cell A, while the image acquisition rate was kept the same, enabling the charging process to be captured with much finer temporal resolution.

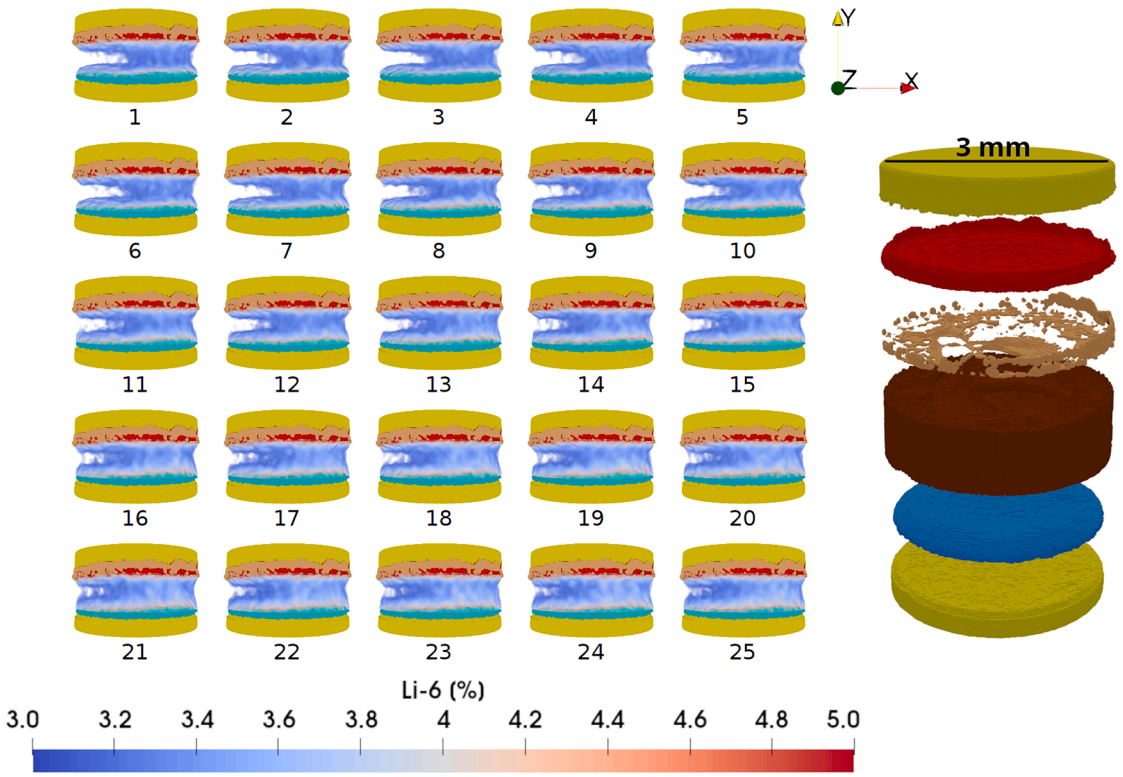

Figure 5. Cell A: Li-6 content in the separator during cycling

The yellow regions are the current collectors, the blue region is the cathode, and the red region is the anode. The numbering refers to the points marked in Figure 4. Note the asymmetry present in the Li-6 concentration, where the concentration is higher on the right side of the separator.

Figure 7 reveals that the attenuation of the cathode in cell B decreased monotonously during the charging (delithiation of the cathode). Furthermore, already during this first cycle, an increase in the neutron attenuation in the separator can be seen in Figure 7 (marked by dashed lines). This implies an increase in the Li-6 concentration in the separator, like the increase observed in the separator of cell A during repeated cycling.

When considering the lithiation of the anode, an increase in the neutron attenuation can be seen at both the anode-separator interface as well as at the interface between the anode and the current collector. In both regions, the attenuation increase appears to be reversible, as the attenuation decreases in both regions after approximately 8 h. This corresponds to the end of charging and the start of discharging, suggesting that the process behind the increase in neutron attenuation should be linked to the formation of LiIn alloy at the anode. In contrast to the behavior at the interfaces, the neutron attenuation of the bulk of the anode decreases during the lithiation, which further suggests that metallic indium in the anode is being lithiated.

For cell B, a total of 24 tomographies were acquired. Of these, 20 correspond to the initial charging process (the first half-cycle). During this initial charging, natural lithium will have been removed from the cathode and, more importantly, no new lithium should have been inserted into the cathode from the anode after diffusion through the Li-7-enriched separator. Therefore, it is possible to quantify the lithium content in the cathode and, thus, the state of lithiation from the neutron attenuation values (see methods section), which was not possible for cell A due to the mixing of the natural lithium and Li-7 from the separator with charge cycling.

Figure 8 shows the calculated average lithiation state of the cathode, based on the average neutron attenuation of the segmented cathode volume and the assumption that the cathode was fully lithiated when the charge began, i.e., that the lithiation was initially 100%. It is seen that the calculated degree of lithiation reached a minimum at about 8 h, before increasing again, and that the decrease was non-linear over time (under the constant charge rate). Theoretically, the degree of lithiation should decrease linearly during charging under a constant charge rate, as the change in lithium concentration should be proportional to the current. One possible explanation for this inconsistency, between the expected linear trend and the non-linear trend seen in Figure 8, could be a change in the Li-6:Li-7 ratio in the SE of the cathode due to the different lithium isotope compositions of the NCM and SE. This scenario is represented in the different curves shown in Figure 8 and is discussed in more detail later.

The degree of lithiation in the cathode can also be calculated as a function of the distance from the cathode current collector, to observe how the lithium concentration changed throughout the depth of the cathode during charging. Figure 9 presents the calculated lithium content in the cathode as a

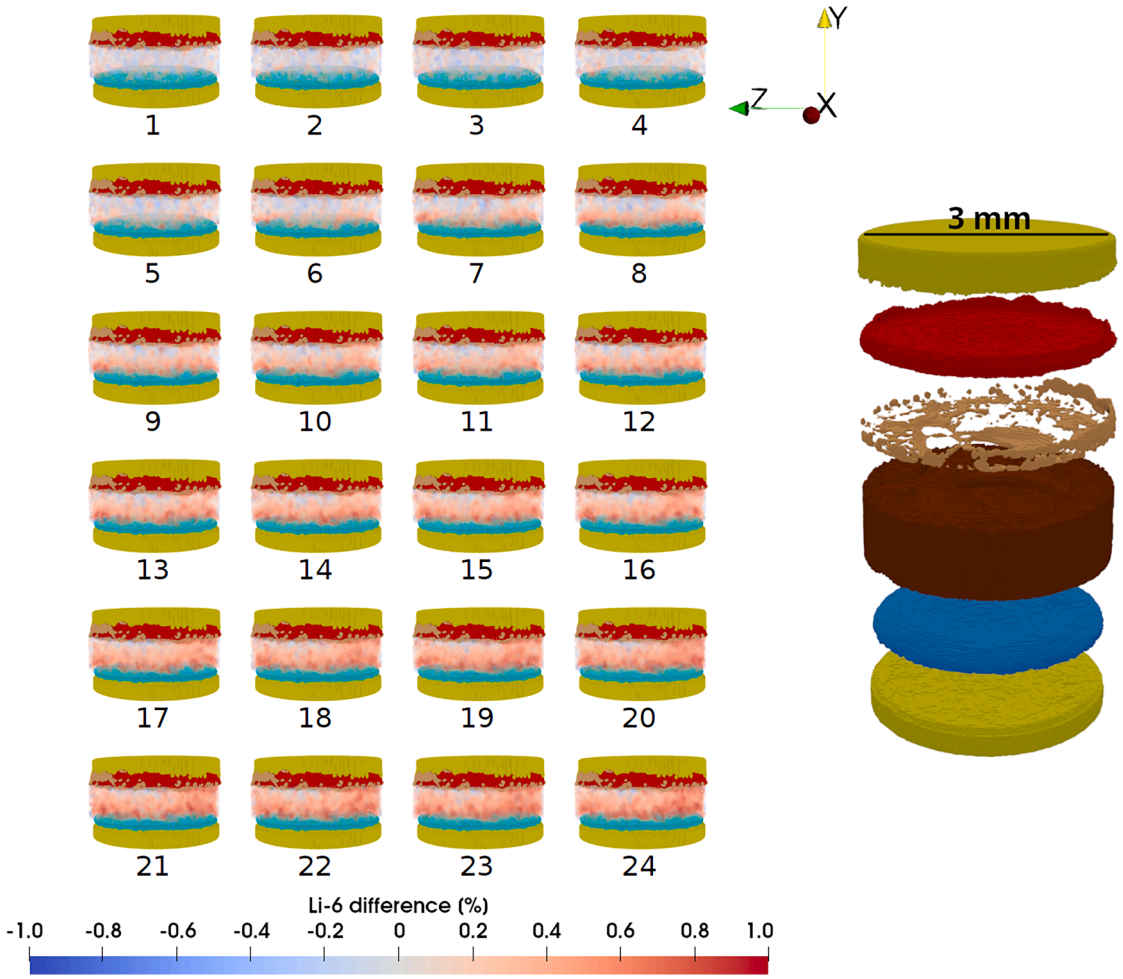

Figure 6. Cell A: Change in Li-6 relative to the initial state in the separator during cycling

The numbering refers to the interval between the steps marked in Figure 4 and Figure 5 (i.e. image 1 refers to the interval between steps 1 and 2). Unlike Figure 5, there is significantly less asymmetry in the change in Li-6 vs. the absolute amount of Li-6, revealing that the entire separator participates in the lithium ion transport process. Note that the orientation of the volumes is different compared to Figure 5, as indicated by the coordinate axes.

function of the distance from the cathode current collector for each time step, normalized relative to the initial state to remove the influence of the initial variability in lithium content. This highlights that the lithium in the cathode was depleted from the side closest to the separator first, with a delithiation front that moved deeper into the cathode, toward the current collector, as the charging progressed. At the change from delithiation to lithiation, the lithium content in the layers of the cathode closest to the current collector began to increase again, while the lithium concentration remained low at the cathode-separator interface.

To further explore the spatial variability of the delithiation process, the reconstructed 4D data are reported in Figure 10, highlighting how the lithium is inhomogeneously distributed throughout the cathode in the early stages of delithiation. Figure 10 shows that the delithiation initiated at the center of the cathode and progressed deeper into the cathode while spreading further radially, revealing the 4D nature of the delithiation process that occurs in the cathode during charging. This shows that the commonly held assumption of a 1D delithiation process is not necessarily sufficient to fully describe the lithiation and delithiation processes in ASSBs. Instead, the lithium transport process likely depends on the structural and compositional heterogeneity of the material as well as the morphology of the electrodes and the shape of the battery cell.

DISCUSSION

The study of cell A revealed the spatiotemporal inhomogeneity of the lithium ion diffusion process in the separator as well as the lithiation-induced formation of LiIn alloy in the anode. In the study of cell B, further indications of structural changes in the anode were seen and the 4D nature of the delithiation of the cathode upon charging was characterized. The delithiation front in cell B was found to be inhomogeneous throughout the depth of the cathode as well as in the radial direction. These topics

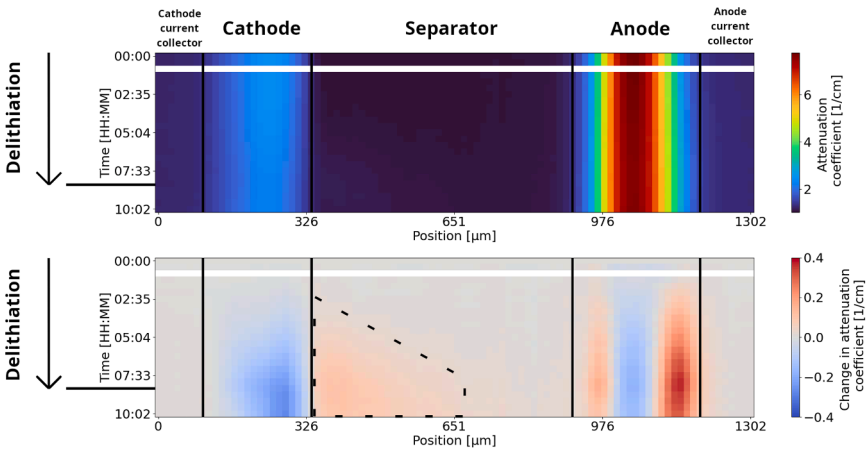

Figure 7. Cell B: Intensity plots of the neutron attenuation coefficient and the change in neutron attenuation coefficient

The top panel shows the neutron attenuation coefficient, and the bottom panel shows the change in neutron attenuation coefficient relative to the initial state. The data are given as a function of the position along the cell symmetry axis, measured from the cathode current collector and the time from the start of the tomographic scans. The delithiation of the cathode stops after approximately 8 h, marked by the horizontal line on the time axis. The delithiation of the cathode causes the Li-6 concentration in the separator to increase over time, seen in the region marked by dashed lines. Due to an issue with data acquisition, one time step is missing from the reconstructed time series, at 1 h into the measurements.

are discussed further in the following and put into context with respect to previous work. The limits and advantages of the methods used to obtain the results are also discussed.

Following previous work (e.g., Bradbury et al.[5,6]), this study employed different concentrations of the Li-6 and Li-7 isotopes to enable mapping of lithium ion diffusion processes based on their different neutron attenuations. The purpose of isotope contrast enhancement, when studying the lithium ion diffusion processes in batteries with neutron imaging, is to enhance the contrast between the lithium ions that are being transported between the electrodes and the surrounding lithium-containing material, e.g., the separator. The cathodes used in this study consisted of a mixture of 70 wt % NCM and 30 wt % SE, where the NCM was the source of mobile lithium and the SE provided ionic transport paths between the NCM particles. As both components contain lithium, lithium ion exchange between the SE particles and the NCM is to be expected and is beneficial to the battery operation, as the SE particles increase the overall ionic conductivity of the cathode. However, the lithium contained in the NCM particles had a different isotopic content than the lithium in the SE, as the SE was synthesized to have a greater percentage of Li-7 compared to the natural isotope distribution found in the NCM. Considering this difference in lithium isotope distribution in combination with the aforementioned lithium ion exchange, the NCM should, ideally, be entirely depleted of lithium after the initial charge and the SE will contain lithium with some unknown isotope distribution (with a Li-6 concentration between that of the original, Li-7-enriched $^{7}Li_{5.5}PS_{4.5}Cl_{1.5}$, and natural lithium). If this mixing is not accounted for, the natural lithium concentration of the NCM will be overestimated from the neutron attenuation due to the increase in Li-6 concentration of the SE, which raises the neutron attenuation of the cathode in the same way as a higher, partially lithiated fraction of NCM would.

Figure 8 presents the calculated evolution of the state-of-lithiation of the cathode in cell B during the initial charge, based on the change in the average neutron attenuation of the entire cathode volume (see methods section). Assuming that only the natural lithium in the NCM was removed from the cathode during the charge, the state of lithiation was predicted to be around 85% at the end of the initial charge. However, given the theoretical capacity of NCM of 210 mAh/g,[12] the degree of lithiation of the cathode at the end of the first charge should have been about 73%. A possible explanation for this discrepancy is that there was a change in the Li-6:Li-7 ratio in the cathode due to some Li-7 (from the SE), leaving the cathode and being replaced with Li-6 from the natural lithium in the NCM. This would have led to an increase in the Li-6:Li-7 ratio and, thus, a higher neutron attenuation for the same state-of-lithiation. This scenario is discussed further in the following.

The data shown in Figure 6 indicate that the maximum increase in Li-6 in the separator (made from the same SE material as in the cathode) was in the order of 1%, giving an estimate for how much of the Li-7 in the SE material of the cathode was replaced by Li-6. Therefore, the average lithiation of the cathode, as a function of time during the charging, has also been calculated using a 1% greater amount of Li-6 in the SE of the cathode, compared to the initial assumption; this is plotted as the orange line in Figure 8. With this assumption, the estimate of the average degree of lithiation of the cathode at the end of the first charge is about 74%, which is closer to the expected value of 73%. However, with this assumption, the initial lithiation is predicted to have been less than 90%, which is inconsistent with the nominal 100% initial lithiation. This inconsistency, in the initial lithiation state for this scenario compared to the expected, reflects that the SE material in the pristine state should have had its original Li-7 enrichment and that no mixing of the lithium isotopes between the natural lithium in the NCM and the Li-7 in the SE is to be expected to have occurred prior to charging. Therefore, it seems reasonable to conclude that there was a transition between the pristine, non-mixed state (where the NCM had the natural lithium Li-6:Li-7 ratio and the SE in the cathode had its enriched Li-6:Li-7 ratio), and the 1% increase in the Li-6 content of the SE by the end of the charging (which would be consistent with the expected value in the delithiated state). However, it is not possible to determine the actual rate at which the change in the Li-6:Li-7 ratio in the SE took place. Figure 8, therefore, shows the prediction of the lithiation state for this scenario based on a linear interpolation between the two different, previously proposed scenarios; i.e., having an initial state with the Li-7-enriched SE and a final (delithiated) state corresponding to a 1% Li-6 increase in the SE relative to the Li-7-enriched initial state,

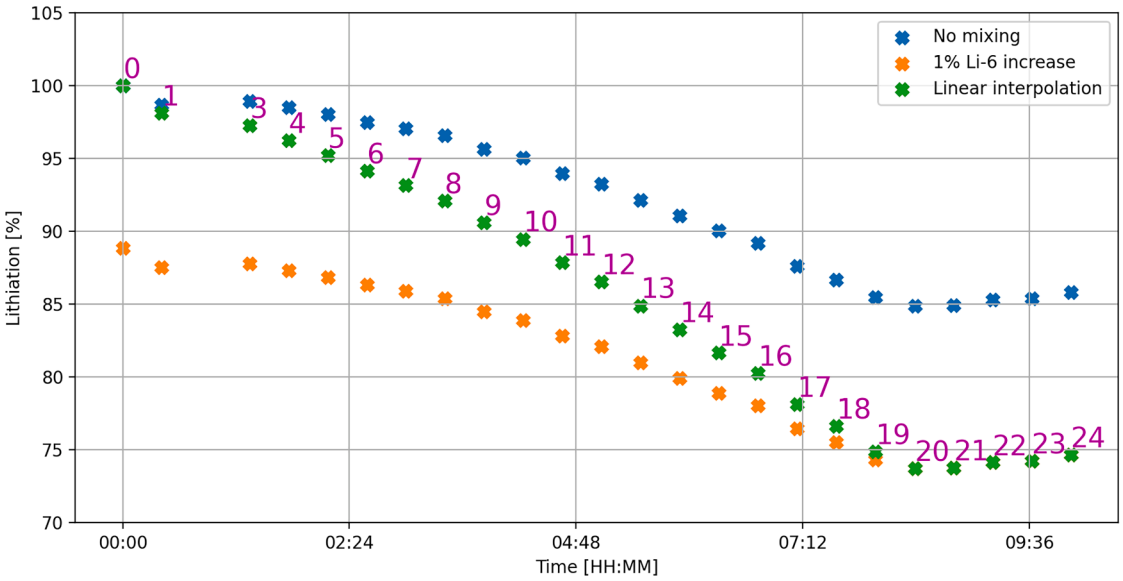

Figure 8. Cell B: Average degree of lithiation in the cathode over time

The average degree of lithiation is calculated from the neutron attenuation values averaged over the cathode volume, as described in the methods section. Each data point corresponds to one tomography acquisition. Three scenarios are presented for the lithiation variation over time, which are described further in the discussion section. These scenarios are based on (1) the assumption of no lithium isotope mixing between the SE and NCM in the cathode (no mixing: blue); (2) a 1% increase in the proportion of Li-6 in the SE of the cathode (consistent with the maximum Li-6 increase found in Figure 6) associated with Li-7 leaving the SE in the cathode (1% mixing, orange); (3) a linear interpolation from scenario (1) to scenario (2) as a function of time (green). The minima in lithiation at point 20 at around 8 h from the start of the measurements, seen for all scenarios, and the slight increase in lithiation afterward correspond to the end of the charging (delithiation of the cathode) and subsequent change to discharging (lithiation of the cathode).

with a linear transition between the two states as a function of time.

It is noted that the estimation of the average lithiation in the cathode is more difficult if the cycling continues and the cathode is lithiated during discharge with excess Li-7 from the separator diffusing into the cathode. This Li-7 would contribute to the lithiation of the cathode without increasing the neutron attenuation as significantly as if natural lithium, with more Li-6, were added to the cathode. Thus, the lithiation of the cathode would be underestimated from the neutron attenuation data. As there is no way to verify whether this is happening upon lithiation of the cathode, it is not possible to estimate the cathode lithiation beyond the initial delithiation.

To fully account for the mixing phenomenon described above, spatiotemporal concentration maps such as those in Figure 10 should be produced for the three phases whose relative amounts will vary over time: in the current case, these phases are the Li-6 and Li-7 (in both the NCM and SE fractions of the cathode) and the Li-depleted NCM in the cathode. This mapping can only be based on a single value of the neutron attenuation per voxel plus the (known) volume fractions of SE and NCM present in the cathode. At best, this provides two equations, meaning that at least one more correlation would be needed to solve for the different lithium isotope concentrations. Thus, it can be concluded that, if isotope contrast enhancement is used, quantification of the lithium isotope distribution in battery electrodes from neutron tomography data can only be performed for the initial half-cycle, after which the introduction of a lithium-depleted phase prevents the isotope distribution and, therefore, the local lithiation state from being quantified.

If no isotope contrast enhancement is used for the SE, the issue of lithium isotope mixing is resolved, as the ratio between Li-6 and Li-7 is fixed. This would allow the state of lithiation of the cathode to be quantified at the expense of reducing the contrast between the cathode and the separator, making the image segmentation process more difficult. Ultimately, whether or not to use isotope contrast enhancement depends on the purpose of the study. Isotope contrast enhancement provides a means for directly observing lithium ion diffusion through the separator and quantifying the lithium isotope distribution in the separator, but the same isotope contrast enhancement obstructs the quantification of the local state of lithiation in the cathode beyond the initial delithiation.

The 4D neutron imaging data also reveal details on LiIn alloy evolution in the anode, as the neutron attenuation of indium is about three times greater than the neutron attenuation of natural lithium (see methods section), so the two materials and their alloy can be distinguished. The local neutron attenuation coefficient of the anode, shown in Figure 3, was found to decrease in regions of high neutron attenuation (indicative of a high indium content) and increase in regions of comparatively lower neutron attenuation (indicative of a high lithium content) when comparing the first and last time steps for cell A. The equilibration of the neutron attenuation of the anode with charge cycling suggests continuing LiIn alloy formation. As suggested by Aspinall et al.,[13] the formation of LiIn upon lithiation of indium is

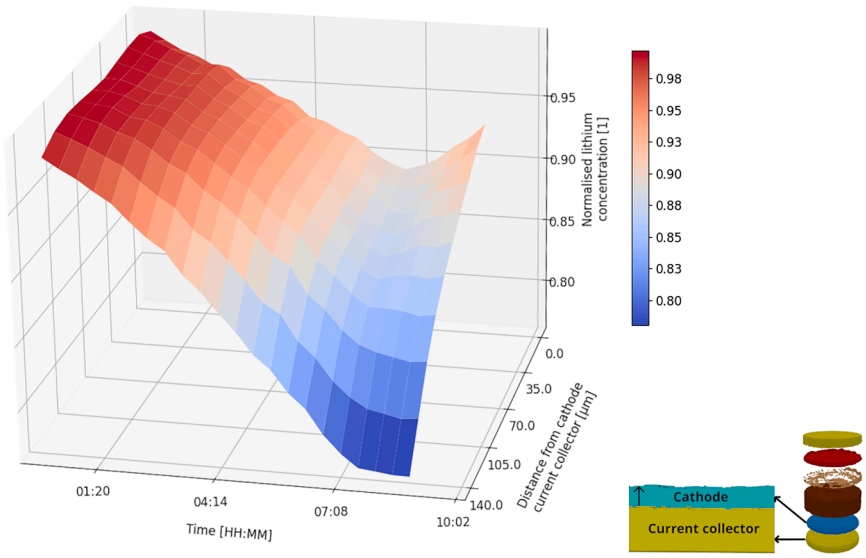

Figure 9. Cell B: Lithium content in the cathode as a function of distance from the current collector and time

The data are normalized relative to the initial state. Note that after 8 h, the current was reversed, leading to the cathode being relithiated.

thermodynamically favorable in comparison to the plating of metallic lithium. Lithium plating may result in the formation of lithium filaments that can cause short-circuits,[14–16] which is a major challenge with lithium metal anodes that is yet to be overcome. Thus, the formation of LiIn alloy is preferable when compared to lithium plating. The continued lithiation of indium is seen to lead to volume expansion of the lithiated regions due to the larger unit cell of the LiIn alloy when compared to metallic indium,[17] thus leading to volume expansion of the anode. The cyclic attenuation variations in the anode of cell A (Figure 4) indicate that the LiIn alloy formation is partly reversible, which would lead to the formation of metallic indium upon discharge and a subsequent local increase in the neutron attenuation coefficient in the delithiated regions. Furthermore, the observed local changes in the neutron attenuation coefficient of the anode of cell A suggest that the formation of LiIn alloy, by solid-state diffusion through *in situ* pressing of lithium and indium foils, appears to cause significant local inhomogeneities in the anode composition, leading to these regions equilibrating through a continued LiIn alloy formation during charging, which is then reversed during discharging. The fact that the LiIn alloy formation is inhomogeneous implies that the process may be difficult to control when pressing the anode *in situ*, potentially causing local inhomogeneities in the lithium concentration and thereby contributing to the electrochemical system deviating from one that may be accurately represented by a 1D model. Therefore, other methods for the manufacture of LiIn anodes may need to be explored, such as melting under an inert atmosphere or *ex situ* pressing.

The better temporal resolution on the first half (charge) cycle for cell B enabled the investigation of the details of the 3D delithiation process. As such, lithium concentration gradients were observed in the cathode of cell B, shown in Figure 10, revealing that the cathode delithiation was a spatially inhomogeneous process with some degree of radial symmetry, as the delithiation appears to have begun at the center of the cathode and progressed radially outward. Furthermore, the delithiation front was shown in Figure 9 to initiate at the interface between the cathode and the separator and progress toward the cathode current collector. When the cathode was lithiated, the lithium concentration front appears to have moved in the opposite direction, i.e., initiating in the depth of the cathode and progressing toward the separator, indicating that, even though delithiation of the cathode during charging occurred from the top and down, lithiation occurred from the bottom and up. An alternative interpretation is that the reversal of the direction of current and, thus, the direction of the electric field with the switch to discharging, caused lithium ions from the top of the cathode to diffuse toward the bottom. Lithiation gradients have previously been observed in the cathodes of ASSBs, where the gradients were found to be dependent on the ratio of active material to solid electrolyte.[18,19] In addition, the direction of the lithium gradient in the cathode, where the lithium content increases closer to the current collector, suggests a comparatively high tortuosity in the cathode.[18] More generally, the observation of lithium concentration gradients in the studied cell suggests that lithium ion diffusion fronts in ASSB electrodes can be present even at low current densities, necessitating further studies about the lithiation of composite cathodes.

To conclude, this paper has presented an *in situ*, operando multimodal neutron and X-ray tomography study of all-solid-state lithium-ion batteries. Using isotope contrast enhancement, the local lithium content evolution in the separator has been quantified in 4D during cycling, revealing the inhomogeneity in lithium ion mobility. This includes revealing inhomogeneous delithiation and relithiation processes in the cathode, leading to the development of lithiation fronts. It has also been highlighted that, although the isotope substitution enhances the contrast in the neutron tomographies and allows for the lithium content in the separator to be quantified, the mixing of the lithium isotopes that occurs as the cell is alternately charged and discharged prevents quantification of the lithiation of the cathode beyond the initial delithiation. It can be concluded that isotope contrast enhancement with neutron imaging is a valuable tool for the study of lithium ion diffusion through the separator of solid-state batteries but presents issues for the quantification of the local lithiation state in the cathode. The neutron tomography data also revealed periodic changes in the neutron attenuation of the LiIn anode, suggesting that the composition of the anode changed during cycling. These changes could either be due to an inhomogeneous alloy formation on assembly that caused the composition of the anode to locally equilibrate when the cell was cycled or due to the LiIn alloy decomposing

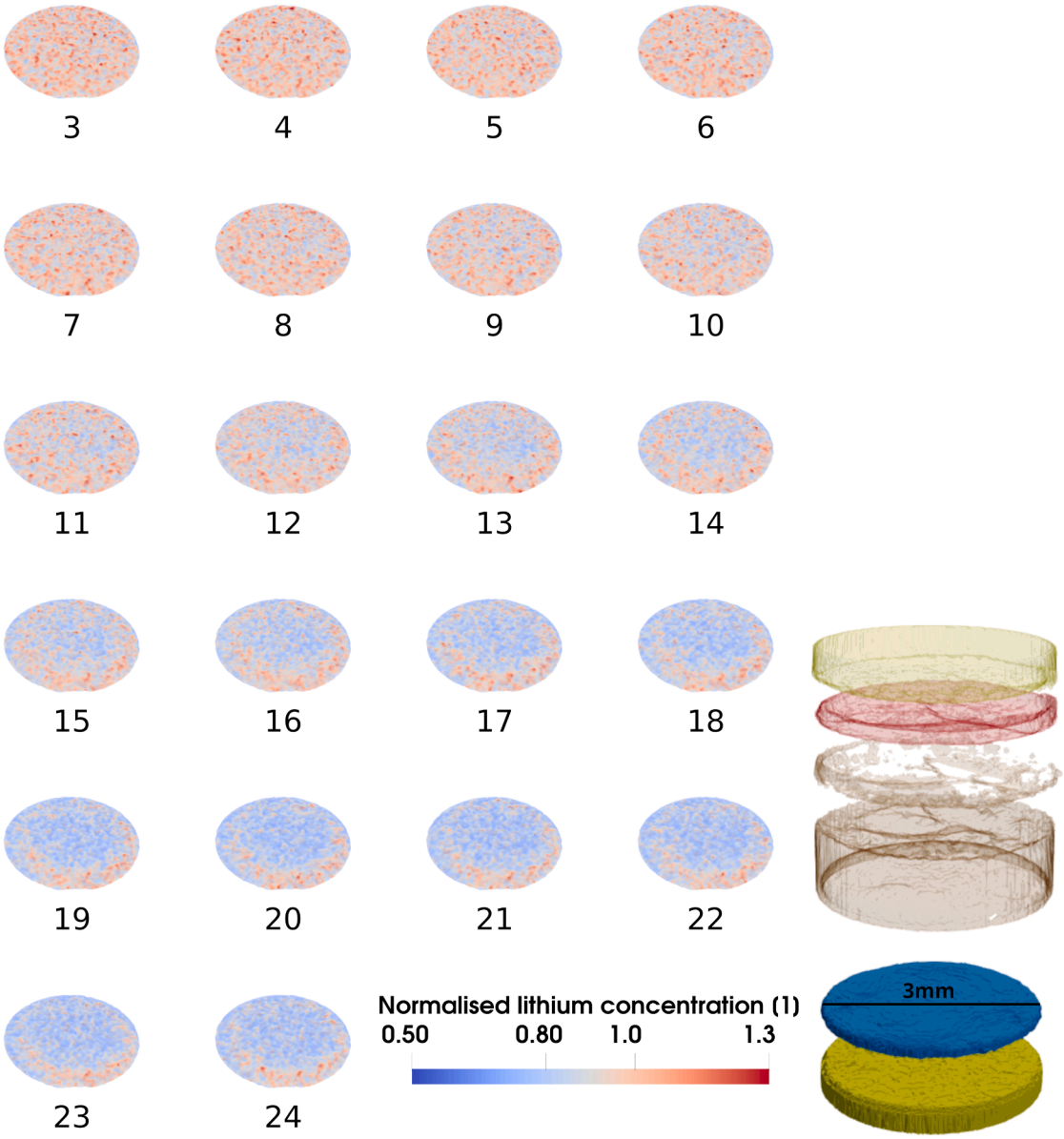

Figure 10. Cell B: Normalized lithium content in the cathode

The data are shown from the first hour (step 3) of charging to 10 h after the start of the charging (step 24). The cell is switched from charging to discharging after 8 h (step 20). The numbering is consistent with the data points shown in Figure 8.

into lithium and indium and subsequently realloying as LiIn, depending on whether the cell is being discharged or charged.

The simultaneous X-ray and neutron tomography imaging used in this study has enabled the successful segmentation of the battery components and the identification of lithium-rich regions in the battery. However, it is noted that cone beam artifacts in the X-ray tomography images, due to the highly X-ray attenuating indium, prevented the use of these data for X-ray-based quantification of the processes in the battery. If the quality and resolution of the X-ray tomographies were improved, the use of such multimodal neutron and X-ray tomography could be enhanced to further understand the electrochemo-mechanical processes in all-solid-state batteries, such as quantification of lithiation-induced local deformations coupled to quantified 3D lithium concentration measurements.

METHODS

Synthesis of $^{7}Li_{5.5}PS_{4.5}Cl_{1.5}$

All synthesis steps were performed under inert condition (O_2 < 0.1 ppm, H_2O < 0.5 ppm). The $^{7}Li_{5.5}PS_{4.5}Cl_{1.5}$ was synthesized by a solid-state synthesis route as previously reported.[20] A stoichiometric amount of lithium chloride (^{7}LiCl, Sigma-Aldrich), lithium sulfide ($^{7}Li_2S$, Sigma-Aldrich), and diphosphorus

Table 1. Parameters for the neutron and X-ray imaging setup

	Neutrons	X-rays
Source-object distance (sod)	10,000 mm	89 mm
Source-detector distance (sdd)	10,005 mm	573 mm
Pinhole diameter	30 mm	–
Image size	1,024 × 1,024	1,712 × 2,096
Collimation ratio	333	–
Current	–	80 μA
Voltage	–	100 kV
Number of projections	799	799
Averaging	3	7
Binning	2	–
Exposure	0.6 s	–
Frame rate	–	4 s^{-1}

pentasulfide (P_2S_5, Sigma) were hand ground with a mortar and pestle for 15 min. The resulting mixture was densified into pellets and put in a silica ampule with carbon coating, which was then sealed under vacuum. In the first reaction step, the ampule was heated at 100°C/h to 450°C and kept there for 72 h, followed by natural cooling after the reaction. The ampule was then opened and the obtained pellets were hand ground for 15 min. The powder was pressed into pellets and the first reaction step was repeated. After the second heating step, the pellets were ground and the powder was characterized using X-ray diffraction and impedance spectroscopy.

X-ray diffraction

Phase purity of the synthesized $^7Li_{5.5}PS_{4.5}Cl_{1.5}$ with different particle sizes was analyzed by X-ray powder diffraction using a StadiP from STOE in Debye-Scherrer geometry with Cu-K_α radiation (λ_1 = 1.545051 Å). The samples were analyzed in sealed 0.5 mm capillaries. The measurements were taken over an angle range of 2θ = 10°–70° with a step size of 0.1° and 15 s per measurement.

EIS

To measure the ionic conductivity of $^7Li_{5.5}PS_{4.5}Cl_{1.5}$, electrochemical impedance spectroscopy (EIS) was performed. For this measurement, a sample of 200 mg of $^7Li_{5.5}PS_{4.5}Cl_{1.5}$ was densified in an airtight, custom-made press cell[21] with a uniaxial pressure of 380 MPa for 3 min. The EIS measurement was performed at 25°C with a Biologic VMP 300 potentiostat at a perturbation amplitude of 10 mV and in a frequency range from 10 mHz to 7 MHz.

Preparation of electrode composites

Cathode composites were prepared by mixing lithium nickel cobalt manganese oxide $LiNi_{0.83}Co_{0.11}Mn_{0.06}O_2$ (NCM83, MSE supplies, dried overnight in a B-585 oven [Büchi] in dynamic vacuum at 250°C) and the respective $^7Li_{5.5}PS_{4.5}Cl_{1.5}$ in a weight ratio of 70:30. The two components were transferred into a 15 mL ZrO_2 cup with 3 mm sized zirconia spheres and mixed using a frequency ball mill (Fritsch pulverisette 23 Mini Mill) at a frequency of 15 Hz for 15 min.

Electrochemical cell assembly

The cell casing was made from aluminum alloy EN AW-7075 coated on the inner surface with a layer of alumina to prevent short-circuits. The casing had an inner diameter of 3 mm and an outer diameter of 4 mm. Steel pins were used to connect the cell to a potentiostat (Gamry Interface 1000) during cycling, from which the current supplied to the cell could be controlled. Two samples were produced and analyzed with the imaging parameters listed in Table 1.

For each cell, ca. 7.8 mg of $^7Li_{5.5}PS_{4.5}Cl_{1.5}$ (the separator) was placed in the cell casing. A handpress was used to press the separator between the two stainless steel stamps in a uniformly distributed layer. One of the steel stamps was removed, and 3.2 mg of the cathode composite, corresponding to an area loading of 6.4 mAh cm^{-2}, was placed above the separator. Particular attention was given to ensure an even and complete coverage of the composite on the separator. The separator and the composite layer were densified within the cell casing between the steel stamps with a handpress at a pressure of 100 MPa for 3 min. After pressing, an indium foil (chemPUR, 100 μm thickness, 99.99%) of 3 mm diameter was placed on the separator, followed by 0.1 mg of lithium (Li, abcr, 99.8%), previously pressed to a foil. The cell was closed by inserting two steel pins at each end of the cell housing, which, together with a pair of internal o-rings, created an airtight environment. For the electrochemical measurements, a stack pressure of 50 MPa was applied and held for 6 h at 25°C for equilibration.

Neutron and X-ray tomography imaging

Both cells were measured operando with neutron and X-ray tomography at the Institut Laue-Langevin, Grenoble, France, using the instrument NeXT.[8] The cold neutron spectrum at NeXT peaks at 11 meV; thus, the attenuation cross sections are evaluated at this energy. The other imaging parameters are given in Table 1.

The first cell (cell A) was cycled with a current density of 1.58 mA/cm^2 (C-rate ca. C/4) in the voltage interval 3.7–2.0 V vs. In/LiIn. Neutron and X-ray tomographies were acquired simultaneously with an acquisition time of 25 min per tomography, using a 21 × 21 μm^2 pixel size for the X-ray tomographies and a 14 × 14 μm^2 pixel size for the neutron tomographies, resulting in voxel sizes of the reconstructed volumes of 21 × 21 × 21 and 14 × 14 × 14 μm^3, respectively. The neutron tomography system is an infinity corrected setup mounting a 55 mm heliflex to a 50 mm Canon f./1.2 objective lens, a Hamamatsu Orca 4V3 (pixel size 6.5 μm, demagnified to 7.15 μm and binned 2), and a 20 μm Gadox scintillator. In total, 25 tomographies, corresponding to 10 h of cycling and 7 stages of either charge or discharge, could be reconstructed from the measurements of cell A.

The second cell (cell B) was cycled at a lower current density compared to cell A, 0.40 mA/cm^2 (C-rate ca. C/25), but using the same voltage range as cell A, i.e., cycling between 3.7 V and 2.0 V vs. In/LiIn. Cell B failed to reach the upper cutoff voltage due to a time limit of 7 h set for the cycling, leading to a maximum charge voltage of approximately 3.36 V for the first charge cycle and 3.56 V for the subsequent cycles. Twenty-four simultaneously acquired neutron and X-ray tomographies, each with an acquisition time of 25 min, were acquired of cell B, capturing

Table 2. Values of the total neutron cross section for a neutron energy of 11 meV as obtained from the JANIS library[24]

Isotope	σ_i [b]	Source
Li-6	1424.38	ENDF/B-VIII.0[26]
Li-7	1.20	ENDF/B-VIII.0[26]
Ni-58	31.73	ENDF/B-VIII.0[26]
Ni-60	4.75	ENDF/B-VIII.0[26]
Ni-61	12.70	ENDF/B-VIII.0[26]
Ni-62	32.44	ENDF/B-VIII.0[26]
Co-59	62.50	ENDF/B-VIII.0[26]
Mn-55	22.28	ENDF/B-VIII.0[26]
O-16	4.07	ENDF/B-VIII.0[26]
P-31	4.51	ENDF/B-VIII.0[26]
S-32	1.81	ENDF/B-VIII.0[26]
Cl-nat	74.03	CENDL-3.2[27]
In-115	303.45	ENDF/B-VIII.0[26]
Li-nat	109.22	ENDF/B-VIII.0[26]

Note that the total neutron cross section for Li-nat is calculated from the values of the cross sections of Li-6 and Li-7, together with the relative abundances of both isotopes.[28]

the first charge cycle plus four tomographies at the start of the subsequent discharge cycle. The slower cycling rate resulted in a significantly higher relative temporal resolution of the imaging compared to cell A, at the expense of only recording the first charge cycle completely.

Methodology for quantification of lithium content

For the acquired neutron radiographies, the recorded intensity, I, is modeled using the Beer-Lambert law for attenuation,[22]

$$I = I_0 e^{-\mu \ell} \quad \text{(Equation 1)}$$

where I_0 is the incident beam intensity, μ is the linear attenuation coefficient, and ℓ is the path length through the sample. After reconstruction, the voxel values in a tomography are assumed to be proportional to the linear attenuation coefficient. The neutron attenuation coefficient, μ, can be modeled as,[23]

$$\mu = \sum N_i \sigma_i \quad \text{(Equation 2)}$$

where N_i is the number density of element i (considering different isotopes), and $\sigma_i(\lambda)$ is the corresponding total neutron cross section, defined as $\sigma_i(\lambda) = \sigma_{i,sc}(\lambda) + \sigma_{i,a}(\lambda)$,[23] where $\sigma_{i,sc}(\lambda)$ denotes the scattering cross section and $\sigma_{i,a}(\lambda)$ denotes the neutron absorption cross section; both are dependent on the neutron wavelength λ. The wavelength-dependent cross sections for neutrons are available from the JANIS library,[24] and the relevant cross sections for this work are given in Table 2. For a molecule, consisting of i different elements, the number density of the i:th element is given by,[25]

$$N_i = \frac{n_i \rho}{M} N_A \quad \text{(Equation 3)}$$

where n_i is the number of atoms of element i in the molecule, ρ is the density of the compound in g/cm^3, M is the molecular mass in g/mol, and N_A denotes the Avogadro number. Considering a mixture of j different compounds, Equation 2 can be generalized to,[23,25]:

$$\mu_j = \sum_i \frac{\rho_j \sigma_i n_i}{M_j} N_A \alpha_j \quad \text{(Equation 4)}$$

where α_j is the volume fraction of constituent j, which can be calculated from the weight fraction as $w_j = \frac{\rho_j}{\rho_{mix}} \alpha_j$, where ρ_j is the density of constituent j, ρ_{mix} is the density of the mixture, and w_j is the weight fraction of constituent j. Using Equation 4, it is possible to solve for the number of atoms n_j, once the voxel values of the reconstructed tomographies have been rescaled to represent the attenuation coefficient in each voxel.

Calculation of lithium isotope distribution

Assuming that the Beer-Lambert law holds for the attenuation, the voxel value v in each reconstructed tomography is assumed to be proportional to the attenuation coefficient μ in that voxel, according to:

$$v = \alpha \mu + \beta \quad \text{(Equation 5)}$$

where α and β are unknown proportionality constants. By approximating the attenuation coefficient of the surrounding air as being equal to zero, the constant β can be found from the voxel values of the region outside of the cell casing. For the constant α to be determined, the value of the attenuation coefficient has to be estimated for some region of the sample.

Since the objective of the analysis performed for cell A is to investigate the lithium flux through the separator, the cathode is chosen as the reference point to define α. Once both coefficients are known, the reconstructed tomography data can be converted using Equation 5 such that the value in each voxel corresponds to the neutron attenuation coefficient in that voxel.

To determine the amount of lithium in the separator, it is assumed that the total amount of Li-6 and Li-7 is equal to 5.5, as given by the chemical composition of the SE, i.e.,

$$n_{Li_6} + n_{Li_7} = 5.5 \quad \text{(Equation 6)}$$

Assuming the data have been normalized such that the value in each voxel corresponds to the linear attenuation coefficient, Equation 4 can be used along with the compositional constraint in Equation 6 to define a linear system of equations in matrix form in the compositions n_{Li_6} and n_{Li_7}:

$$\begin{bmatrix} \frac{\rho_{SSE}}{M_{SSE}} N_A \sigma_{Li_6} & \frac{\rho_{SSE}}{M_{SSE}} N_A \sigma_{Li_7} \\ 1 & 1 \end{bmatrix} \begin{bmatrix} n_{Li_6} \\ n_{Li_7} \end{bmatrix} = \begin{bmatrix} \mu - \sum_i \frac{\rho_{SSE} \sigma_i n_i}{M_{SSE}} N_A \\ 5.5 \end{bmatrix} \quad \text{(Equation 7)}$$

where the sum over i denotes summation over all non-lithium atoms in the SE, i.e., phosphorus, sulfur, and chlorine, which remain stationary in the SE but still contribute to the measured neutron attenuation. ρ_{SSE}, M_{SSE}, and N_A denote the density of the SE, the molar mass of the SE, and Avogadro's number, respectively. The system of equations from Equation 7 is obtained for each voxel in the region of interest, which can be assembled into a single sparse matrix equation and is solved using a sparse matrix solver from SciPy.[29]

A similar methodology is employed to estimate the state of charge in the cathode of cell B, which is complicated by the fact that the cathode consists of a mixture of SE and NCM. To obtain a well-posed problem, it is assumed that only the lithium in the NCM particles is mobile and that the lithium isotope distribution in the SE is constant. Assuming that the reconstructed tomography data are normalized such that the voxel values in the region corresponding to the cathode represent the linear attenuation coefficient in each voxel, the lithium content, which for fully lithiated NCM83 is one mole of lithium per mole of NCM83, can be calculated using Equation 4 as:

$$n_{Li_{nat}} = \frac{M_{NCM}}{\rho_{NCM}\sigma_{Li_{nat}}N_A\alpha_{NCM}}\left(\mu - \sum_j\sum_i \frac{\rho_j\sigma_i n_i}{M_j}N_A\alpha_j\right). \quad \text{(Equation 8)}$$

Here, the sum over j corresponds to a sum over the different constituents of the cathode, i.e., the NCM and the SE. The summation index i corresponds to the different atoms in the NCM and the SE, excluding the natural lithium in the NCM. In Equation 8, μ refers to the attenuation coefficient, calculated in every voxel of the cathode using the neutron tomographies.

RESOURCE AVAILABILITY

Lead contact

Requests for further information and resources should be directed to the lead contact, Philip Vestin (philip.vestin@solid.lth.se).

Materials availability

This study did not generate new materials.

Data and code availability

- All data from the experiment will be available under https://doi.org/10.5291/ILL-DATA.1-06-12 after the data embargo period. Before the end of the embargo period, all data reported in this paper will be shared by the lead contact upon request.
- This paper does not report original code.
- Any additional information required to reanalyze the data reported in this paper is available from the lead contact upon request.

ACKNOWLEDGMENTS

The authors would like to acknowledge the NeXT-ILL beamline staff. Beam time was provided by Ni-Matters, and the project is funded by Vetenskapsrådet (project 2021-05989). We also gratefully acknowledge the financial support by the German Federal Ministry of Research and Education (BMBF) within the project ANISSA (FKZ: 05K22PMA). We would also like to acknowledge the mechanical workshop of the Institute of Inorganic and Analytical Chemistry at the University of Münster and, in particular, Frederik Henrichmann for developing and manufacturing the cell casing.

AUTHOR CONTRIBUTIONS

Data acquisition, N.K., O.S.-P., and A.T.; data analysis, P.V., writing – original draft, P.V. and E.S.; electrochemical cell construction, E.S.; data interpretation, all authors; supervision, S.H., R.W., and W.G.Z.; and writing – review & editing, all authors.

DECLARATION OF INTERESTS

The authors declare no competing interests.

Received: September 3, 2025
Revised: November 21, 2025
Accepted: January 16, 2026
Published: February 18, 2026

REFERENCES

1. Kodama, M., Komiyama, S., Ohashi, A., Horikawa, N., Kawamura, K., and Hirai, S. (2020). High-pressure in situ X-ray computed tomography and numerical simulation of sulfide solid electrolyte. J. Power Sources *462*, 228160. https://doi.org/10.1016/j.jpowsour.2020.228160.
2. Lübke, E., Helfen, L., Cook, P., Mirolo, M., Vinci, V., Korjus, O., Fuchsbichler, B., Koller, S., Brunner, R., Drnec, J., and Lyonnard, S. (2024). The origins of critical deformations in cylindrical silicon based Li-ion batteries. Energy Environ. Sci. *17*, 5048–5059. https://doi.org/10.1039/D4EE00590B.
3. Ziesche, R.F., Arlt, T., Finegan, D.P., Heenan, T.M.M., Tengattini, A., Baum, D., Kardjilov, N., Markötter, H., Manke, I., Kockelmann, W., et al. (2020). 4D imaging of lithium-batteries using correlative neutron and X-ray tomography with a virtual unrolling technique. Nat. Commun. *11*, 777. https://doi.org/10.1038/s41467-019-13943-3.
4. Ziesche, R.F., Kardjilov, N., Kockelmann, W., Brett, D.J.L., and Shearing, P.R. (2022). Neutron imaging of lithium batteries. Joule *6*, 35–52. https://doi.org/10.1016/j.joule.2021.12.007.
5. Bradbury, R., Kardjilov, N., Dewald, G.F., Tengattini, A., Helfen, L., Zeier, W.G., and Manke, I. (2023). Visualizing Lithium Ion Transport in Solid-State Li–S Batteries Using 6Li Contrast Enhanced Neutron Imaging. Adv. Funct. Mater. *33*, 2302619. https://doi.org/10.1002/adfm.202302619.
6. Bradbury, R., Dewald, G.F., Kraft, M.A., Arlt, T., Kardjilov, N., Janek, J., Manke, I., Zeier, W.G., and Ohno, S. (2023). Visualizing Reaction Fronts and Transport Limitations in Solid-State Li–S Batteries via Operando Neutron Imaging. Adv. Energy Mater. *13*, 2203426. https://doi.org/10.1002/aenm.202203426.
7. Magnier, L., Lecarme, L., Alloin, F., Maire, E., King, A., Bouchet, R., Tengattini, A., and Devaux, D. (2021). Tomography Imaging of Lithium Electrodeposits Using Neutron, Synchrotron X-Ray, and Laboratory X-Ray Sources: A Comparison. Front. Energy Res. *9*, 657712. https://doi.org/10.3389/fenrg.2021.657712.
8. Tengattini, A., Lenoir, N., Andò, E., Giroud, B., Atkins, D., Beaucour, J., and Viggiani, G. (2020). NeXT-Grenoble, the Neutron and X-ray tomograph in Grenoble. Nucl. Instrum. Methods Phys. Res. Sect. A Accel. Spectrom. Detect. Assoc. Equip. *968*, 163939. https://doi.org/10.1016/j.nima.2020.163939.
9. Roubin, E., Andò, E., and Roux, S. (2019). The colours of concrete as seen by X-rays and neutrons. Cement Concr. Compos. *104*, 103336. https://doi.org/10.1016/j.cemconcomp.2019.103336.
10. Whang, G., Huang, J., Le Pham, P.N., Kraft, M.A., and Zeier, W.G. (2025). Not All Lithium–Indium Counter Electrodes Are Made Equal: Probing the Inhomogeneities and Kinetics of Uniaxially Pressed Li–In Counter Electrodes in All Solid-State Batteries. ACS Electrochem. *1*, 249–262. https://doi.org/10.1021/acselectrochem.4c00060.
11. Jeong, W.J., Wang, C., Yoon, S.G., Liu, Y., Chen, T., and McDowell, M.T. (2024). Electrochemical behavior of elemental alloy anodes in solid-state batteries. ACS Energy Lett. *9*, 2554–2563. https://doi.org/10.1021/acsenergylett.4c00915.
12. (2025). High Nickel Ni83 Single crystal NMC Cathode Powder. https://cdn.shopify.com/s/files/1/0722/7785/files/High_Nickel_Ni83_Single_crystal_NMC_data_sheet_MSE_Supplies.pdf?v=1616565677.
13. Aspinall, J., Chart, Y., Guo, H., Shrestha, P., Burton, M., and Pasta, M. (2024). Effect of Microstructure on the Cycling Behavior of Li–In Alloy Anodes for Solid-State Batteries. ACS Energy Lett. *9*, 578–585. https://doi.org/10.1021/acsenergylett.3c02274.

14. Schlenker, R., Stępień, D., Koch, P., Hupfer, T., Indris, S., Roling, B., Miß, V., Fuchs, A., Wilhelmi, M., and Ehrenberg, H. (2020). Understanding the Lifetime of Battery Cells Based on Solid-State Li6PS5Cl Electrolyte Paired with Lithium Metal Electrode. ACS Appl. Mater. Interfaces *12*, 20012–20025. https://doi.org/10.1021/acsami.9b22629.

15. Luo, S., Wang, Z., Li, X., Liu, X., Wang, H., Ma, W., Zhang, L., Zhu, L., and Zhang, X. (2021). Growth of lithium-indium dendrites in all-solid-state lithium-based batteries with sulfide electrolytes. Nat. Commun. *12*, 6968. https://doi.org/10.1038/s41467-021-27311-7.

16. Jing, W., Zou, K., Dai, X., Sun, J., Tan, Q., Chen, Y., and Liu, Y. (2022). Li-Indium alloy anode for high-performance Li-metal batteries. J. Alloys Compd. *924*, 166517. https://doi.org/10.1016/j.jallcom.2022.166517.

17. Zhang, W., Schröder, D., Arlt, T., Manke, I., Koerver, R., Pinedo, R., Weber, D.A., Sann, J., Zeier, W.G., and Janek, J. (2017). (Electro)chemical expansion during cycling: monitoring the pressure changes in operating solid-state lithium batteries. J. Mater. Chem. A Mater. *5*, 9929–9936. https://doi.org/10.1039/C7TA02730C.

18. Stavola, A.M., Sun, X., Guida, D.P., Bruck, A.M., Cao, D., Okasinski, J.S., Chuang, A.C., Zhu, H., and Gallaway, J.W. (2023). Lithiation Gradients and Tortuosity Factors in Thick NMC111-Argyrodite Solid-State Cathodes. ACS Energy Lett. *8*, 1273–1280. https://doi.org/10.1021/acsenergylett.2c02699.

19. Bernges, T., Ketter, L., Helm, B., Kraft, M.A., See, K.A., and Zeier, W.G. (2025). Transport characterization of solid-state Li2FeS2 cathodes from a porous electrode theory perspective. EES Batteries *1*, 172–184. https://doi.org/10.1039/D4EB00005F.

20. Gautam, A., Ghidiu, M., Suard, E., Kraft, M.A., and Zeier, W.G. (2021). On the Lithium Distribution in Halide Superionic Argyrodites by Halide Incorporation in Li7–xPS6–xClx. ACS Appl. Energy Mater. *4*, 7309–7315. https://doi.org/10.1021/acsaem.1c01417.

21. Zhang, W., Weber, D.A., Weigand, H., Arlt, T., Manke, I., Schröder, D., Koerver, R., Leichtweiss, T., Hartmann, P., Zeier, W.G., and Janek, J. (2017). Interfacial Processes and Influence of Composite Cathode Microstructure Controlling the Performance of All-Solid-State Lithium Batteries. ACS Appl. Mater. Interfaces *9*, 17835–17845. https://doi.org/10.1021/acsami.7b01137.

22. Pietsch, P., and Wood, V. (2017). X-Ray Tomography for Lithium Ion Battery Research: A Practical Guide. Annu. Rev. Mater. Res. *47*, 451–479. https://doi.org/10.1146/annurev-matsci-070616-123957.

23. Hussein, E.M.A. (2007). CHAPTER THREE - CROSS SECTIONS. In Radiation Mechanics, E.M.A. Hussein, ed. (Elsevier Science Ltd), pp. 153–245. https://doi.org/10.1016/B978-008045053-7/50004-5.

24. Soppera, N., Bossant, M., and Dupont, E. (2014). JANIS 4: An Improved Version of the NEA Java-based Nuclear Data Information System. Nucl. Data Sheets *120*, 294–296. https://doi.org/10.1016/j.nds.2014.07.071.

25. Hussein, E.M.A. (2007). CHAPTER ONE - MECHANISMS. In Radiation Mechanics, E.M.A. Hussein, ed. (Elsevier Science Ltd). https://doi.org/10.1016/B978-008045053-7/50002-1.

26. Brown, D.A., Chadwick, M.B., Capote, R., Kahler, A.C., Trkov, A., Herman, M.W., Sonzogni, A.A., Danon, Y., Carlson, A.D., Dunn, M., et al. (2018). ENDF/B-VIII.0: The 8th Major Release of the Nuclear Reaction Data Library with CIELO-project Cross Sections, New Standards and Thermal Scattering Data. Nucl. Data Sheets *148*, 1–142. https://doi.org/10.1016/j.nds.2018.02.001.

27. Ge, Z., Xu, R., Wu, H., Zhang, Y., Chen, G., Jin, Y., Shu, N., Chen, Y., Tao, X., Tian, Y., et al. (2020). CENDL-3.2: The new version of Chinese general purpose evaluated nuclear data library. EPJ Web Conf. *239*, 09001. https://doi.org/10.1051/epjconf/202023909001.

28. Royal Society of Chemistry (2024). Lithium - Element information, properties and uses | Periodic Table. https://www.rsc.org/periodic-table/element/3/lithium.

29. Virtanen, P., Gommers, R., Oliphant, T.E., Haberland, M., Reddy, T., Cournapeau, D., Burovski, E., Peterson, P., Weckesser, W., Bright, J., et al. (2020). SciPy 1.0: Fundamental Algorithms for Scientific Computing in Python. Nat. Methods *17*, 261–272. https://doi.org/10.1038/s41592-019-0686-2.